Cobalt Nickel Boride Nanocomposite as High-Performance Anode Catalyst for Direct Borohydride Fuel Cell

Yu-e Duan[a], Sai Li[a,*], Qiang Tan[b,*], Yuanzhen Chen[b], Kunyang Zou[b], Xin Dai[b], Maryam Bayati[c], Ben B. Xu[c], Laurent Dala[c], Terence Xiaoteng Liu[c,*]

[a] *School of Chemistry and Chemical Engineering, Xi'an University of Science and Technology, Xi'an, 710054, China*

[b] *State Key Laboratory for Mechanical Behavior of Materials, School of Material Science and Engineering, Xi'an Jiaotong University, Xi'an, 710049, China*

[c] *Department of Mechanical and Construction Engineering, Faculty of Engineering and Environment, Northumbria University, Newcastle upon Tyne, NE1 8ST, United Kingdom*

*Corresponding authors

Dr. Sai Li
saili@xust.edu.cn
Dr. Qiang Tan
qiangtan@xjtu.edu.cn
Dr. Terence X. Liu
terence.liu@northumbria.ac.uk

Abstract

Similar to MXene, MAB is a group of 2D ceramic/metallic boride materials which exhibits unique properties for various applications. However, these 2D sheets tend to stack and therefore lose their active surface area and functions. Herein, an amorphous cobalt nickel boride (Co-Ni-B) nanocomposite is prepared with a combination of 2D sheets and nanoparticles in the center to avoid agglomeration. This unique structure holds the 2D nano-sheets with massive surface area which contains numerous catalytic active sites. This nanocomposite is prepared as an electrocatalyst for borohydride electrooxidation reaction (BOR). It shows outstanding catalytic activity through improving the kinetic parameters of BH_4^- oxidation, owing to abundant ultrathin 2D structure on the surface, which provide free interspace and electroactive sites for charge/mass transport. The anode catalyst led to a 209 mW/cm^2 maximum power density with high open circuit potential of 1.06 V at room temperature in a miniature direct borohydride fuel cell (DBFC). It also showed a great longevity of up to 45 h at an output power density of 64 mW/cm^2, which is higher than the Co-B, Ni-B and PtRu/C. The cost reduction and prospective scale-up production of the Co-Ni-B catalyst are also addressed.

Keywords: Direct borohydride fuel cell, Borohydride electrooxidation, Cobalt Nickel Boride, Electrocatalyst.

1. Introduction

Hydrogen fueled polymer electrolyte membrane fuel cell (PEMFC) with zero carbon emission is considered as a promising renewable energy source for environmental

remedy [1, 2]. However, hydrogen as fuel imposes storage and transportation risk [3, 4]. Direct borohydride fuel cell (DBFC) by employing KBH_4 solution as fuel, overcomes these issues and concomitantly provides high theoretical open-circuit potential (OCP) of 1.64 V due to high hydrogen content of KBH_4 (7.5 wt%) and its high energy density (6500 Wh/kg) [5]. As shown in Eq (1), the maximum of eight electrons are released during borohydride electrooxidation reaction (BOR) on the DBFC anode side [6].

$$KBH_4 + 8OH^- \rightarrow KBO_2 + 6H_2O + 8e^- \qquad E_0 = -1.24\ V\ vs\ SHE \tag{1}$$

The essential part of DBFC is the high-performance anode catalyst which can efficiently catalyze KBH_4 oxidation with high kinetic parameters of BH_4^- and its low hydrolysis.

A large range of nanomaterials have been currently explored as BOR catalysts, *i.e.* noble metals (Pd, Pt, Au, Os, Ag, and Ru) [7-12], transition metals (Ni, Co, Cu) [13-15], hydrogen storage alloys (AB_5^- and AB_2^- type) [16] and bimetallic catalysts (Pt-Co, Co-W, and Ni-Co) [17-20]. However, among those, only a few catalysts, such as Au or Ag based catalysts [21], have achieved near 100% faraday efficiency (FE), which also considered as BH_4^- oxidation efficiency. Noble metals such as Pt and Pd although show high catalytic activity towards BH_4^- oxidation, but they promote BH_4^- hydrolysis, and as the result decrease FE (releasing between 3 and 6 electrons per borohydride converted) [22, 23]. Hydrogen storage alloys increase FE by inhibiting hydrolysis, but their BOR potential is much lower in comparison with noble metals, which results in low OCP and power output [24]. It is reported that bimetallic or alloy

71 catalysts show higher catalytic activity and better stability than single metal ones
72 which benefit of the merits of each component in the catalyst [25].

73 Recently, Ni, Co-based metals/alloys and borides have attracted considerable
74 attention for the relatively low price, high abundancy and excellent performance in
75 capacitor and catalyst. Wang *et al*. [26] improved the capacitor's performance via
76 tuning the crystalline and electronic structures of bimetallic Co-Ni and MOFs to boost
77 faradaic redox reaction for high energy density. As-obtained Co-Ni-B-S exhibits a
78 high specific capacitance (1281 F/g at 1 A/g), due to the excess S^{2-} formed a smaller
79 nanosheets attached to the surface, which benefit for the electrolyte penetration,
80 facilitate the short ion diffusion pathways and lead to higher energy storage. Masaan
81 *et al*. [27] also found that amorphous Co_2B is an exceptionally efficient electrocatalyst
82 for the oxygen evolution reaction (OER) in alkaline electrolytes, because of the B
83 induces lattice strain in the crystal structure of the metal, which potentially diminishes
84 the thermodynamic and kinetic barrier of the hydroxylation reaction. Tan *et al*. [28]
85 present an amorphous Co-B nanosheet coated Co-Bi (Co-B@Co-Bi) nanocomposite.
86 Benefiting from the unique rich amorphous Co-Bilayer on the surface of Co-B, the
87 Co-B@Co-Bi exhibits extraordinary catalytic activity and good stability toward the
88 OER in 1.0 M KOH. Li *et al*. [29] synthesized amorphous Ni-B nanoparticles as the
89 anode catalyst for DBFC, which exhibited a peak power density of 180 mW/cm^2, and
90 a relatively stable performance for approximately 180 h.

91 A number of 2D materials eg, graphene [30, 31], borophene [32, 33] and MXene
92 [34, 35] have been recognized as materials with high surface area and great electric

conductivity which made them suitable for their application in catalysis. MAB a group of 2D ceramic/metallic boride (instead of C or N in MXenes) materials with similar structure to MXenes, also considered as excellent candidates for electrocatalysis owing to the exceptionally high conductivity, rich interlayer porosity, high surface area and adjustable band gap structure etc. These materials were found to possess high heterogeneous electron transfer (HET) rates, and promising electrocatalytic performances toward hydrogen evolution reaction (HER) and oxygen reduction reaction (ORR) [36], and other electrochemical energy storage systems [37]. However, these 2D sheets tend to stack and the material will lose its desired function.

Herein, we prepared amorphous Co-Ni-B nanocomposite catalyst with a combination of 2D nano-sheets and nanoparticles in the center via a simple potassium borohydride reduction approach. This structure benefits the electrochemical BOR activity, while it prevents the stacking of the 2D structures. Besides, the 2D structure planting on the surface of the nanocomposites, which provides more channels for charge/mass transport and increases the conductivity. The Co-Ni-B catalyst's catalytic activity toward BH_4^- oxidation and the DBFC performance are all well discussed. Electrochemical testing results of binary Co-B, Ni-B and commercially available PtRu/C and Pt/C electrocatalysts are also included in this research as a comparison.

2. Experiments

2.1. Materials and chemicals

Nickel chloride hexahydrate ($NiCl_2 \cdot 6H_2O$, 98 wt%), cobalt chloride hexahydrate ($CoCl_2 \cdot 6H_2O$, 98 wt%), 99.5 wt%), potassium borohydride (KBH_4, 98 wt%),

115 potassium hydroxide (KOH, 90 wt%), lanthanum nitrate hexahydrate
116 ($La(NO_3)_3 \cdot 6H_2O$, 99.9 wt%), nickel nitrates $Ni(NO_3)_2 \cdot 6H_2O$, 99.9 wt%)
117 tetrapropylammonium bromide (TPAB, 98 wt%), tetramethylammonium hydroxide
118 pentahydrate (TMAOH, 99 wt%). Commercial PtRu/C (Pt 40 wt% Ru 20 wt%) and
119 Pt/C (40 wt%) was supplied by Johnson Matthey (shanghai, China). Multi walled
120 carbon nanotubes (MWCNT) was purchased from Tanfeng Tech.Inc (China). Ethanol
121 (99.9 wt%) and hydrochloric acid (HCl, 37 wt%) were obtained from Sinopharm
122 (China). Nafion (D520, 5% solution) was acquired from DuPont Corporation.
123 Polytetrafluoroethylene solution (PTFE, 60 wt%) was acquired from DuPont
124 Corporation (America), nickel foam (thickness =1.7 mm, porosity >95%, Fig. S1)
125 was purchased from Kunshan Maozhen Electronics Co., Ltd (China), it was cleaned
126 carefully by ethanol and deionized water before coating the catalytic ink. The gas
127 diffusion layer (PTFE+Carbon, thickness =0.2±0.05 mm, porosity≈20-25 Vol%) was
128 purchased from Changsha spring new energy technology Co., Ltd (China). O_2 (99.99
129 Vol%) and Ar were supplied by Shaanxi Xinkang Medical Oxygen Co., Ltd (China).
130 Deionized water (18.25 MΩ cm resistivity) was used throughout the experiments. All
131 chemical reagents were used directly without further purification.

132 *2.2. Catalyst synthesis*

133 The catalyst was prepared via a simple potassium borohydride reduction
134 approach using $NiCl_2 \cdot 6H_2O$, $CoCl_2 \cdot 6H_2O$ and KBH_4. 75 mL KBH_4 (0.2 mol/L) was
135 added drop-wisely into 50 mL $CoCl_2 \cdot 6H_2O$ (0.1 mol/L) solution and the dropping rate
136 was 1.0 mL/min, then with vigorous stirring at room temperature (~25 ^oC). After 2 h

stirring, the mixture was transferred into an ice bath. At the same time, further 37.5 mL KBH_4 (0.2 mol/L) and 125 mL $NiCl_2 \cdot 6H_2O$ (0.02 mol/L) with the dropping rate of 1.0 mL/min and 3.3 mL/min were added into the solution while it was stirred vigorously until no gas generated. To ensure a complete reduction, the molar ratio of KBH_4 to Ni and KBH_4 to Co was 3:1. After the reaction was completed, the mixture was filtrated and washed with deionized water and ethanol to remove any residues. Then, the catalyst of Co-Ni-B was obtained by freeze-drying overnight. The catalysts with different molar ratios of Co to Ni were prepared according to the preceding method, and the molar ratio of Co to Ni were 1:1, 1:2, 1:3, 2:1, and 3:1. The preparation procedure was illustrated in Scheme 1. For comparison, Co-B and Ni-B catalysts were synthesized using the procedures.

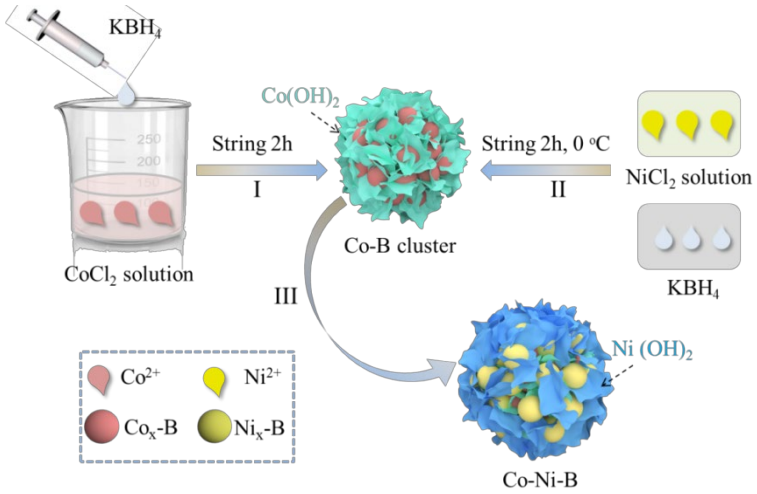

Scheme 1- Synthetic process of the Co-Ni-B catalyst.

The Lanthanum nickel oxide ($LaNiO_3$) as cathode catalyst of DBFC was prepared using the reverse-phase hydrolysis method as described another paper [38]. The $La(NO_3)_3 \cdot 6H_2O$ and $Ni(NO_3)_2 \cdot 6H_2O$ were mixed with 1:1 molar ratio in 50 mL of deionized water, such that the total metal concentration was 9.9 mmol.

Tetrapropylammonium bromide (TPAB) was dissolved into 200 mL of 1 wt% tetramethylammonium hydroxide (TMAOH, PH14) followed by added the metal nitrate solution drop-wisely (2.0 mL/min) into TPAB solution under vigorous stirring. The solution was left stirring for 24 h and then centrifuged for 4 minutes at 8000 rpm resulting in a gelatinous green pellet, followed by washing with deionized water, which resulted in a green colloidal suspension. The colloid was dispersed in 100 mL of deionized water and stored in a freezer for overnight. After freeze-drying, particles consist of lanthanum and nickel hydroxides were calcined at 700 °C for 4 h to form the perovskite phase. The resulting perovskite particles were washed with ethanol and deionized water and vacuum filtered to obtain the final $LaNiO_3$ catalyst.

2.3. Characterization

X-ray diffraction (XRD, Bruker D8 ADVANCE) was used to characterize the crystal structures of samples. The field emission scanning electron microscope (FE-SEM, Zeiss GeminiSEM 500) and high resolution field emission transmission electron microscope (FE-TEM, ThermoFisher Talos-F200X) were employed to characterize the morphology, crystal structure and element distribution of the catalysts. The valence state of elements and elemental composition were tested by X-ray photoelectron spectroscopy (XPS, Thermo Fisher ESCALAB Xi^+, Thermo Fisher technologies, China), the binding energy (BE) was calibrated using C 1s = 284.6 eV as reference. Infrared spectrum (IR, Bruker Vetex 70, Bruker AXS, Germany) was used to detect OH^- functional group in the catalysts. UV Spectrophotometer (Shimadzu UV-2550) was employed to record the ultraviolet-visible (UV-vis) diffuse

reflectance spectra of the catalysts, to characterize the band gap, and $BaSO_4$ as reference sample. Inductively Coupled Plasma Mass spectrometer (NexION 350D ICP-MS, PerkinElmer Co., Ltd, China) was used for element composition analysis. An electrochemical workstation (CHI750d Shanghai Chenhua Instrument Co., Ltd.) was employed to test the half-cell electrochemical oxidation of catalysts. The battery testing system (BTS-5 V 3A, Neware Technology Co., Ltd., Shenzhen, China) was employed to measure the performance of the DBFC.

2.4. Electrochemical Testing

The half-cell electrochemical oxidation reaction of the catalysts was investigated using a CHI750d electrochemical workstation with a conventional three-electrode cell at room temperature (~25 ^{o}C) (Fig. S2). Glassy carbon rotating disk electrode (RDE, diameter=5 mm), Hg/HgO (1 M KOH) and graphite rod electrode were applied as working electrode, reference electrode and the counter electrode, respectively. The catalyst ink was prepared by mixing 5 mg catalyst in 500 μL ethanol and 20 μL Nafion (5 wt%) solution in ultrasonic sound bath for 15 minutes. Then 15 μL of the ink was dropped on the surface of the glassy carbon electrode followed by drying at room temperature to ensure a catalyst loading of 0.735 mg/cm^2. The cyclic voltammograms (CV) were recorded at a range of 0-0.7 V *vs*. Hg/HgO with scan rates of 50 mV/s. The catalysts were coated on a piece of Ni foam (A=1cm^2) for chronoamperometry (CA) testing. The CA curves were recorded at 0.6 V *vs* Hg/HgO, with the catalyst loading of 10 mg/cm^2.

2.5. Electrode preparation and DBFC testing

198 The structure of the DBFC in this work as shown in Fig. 1.

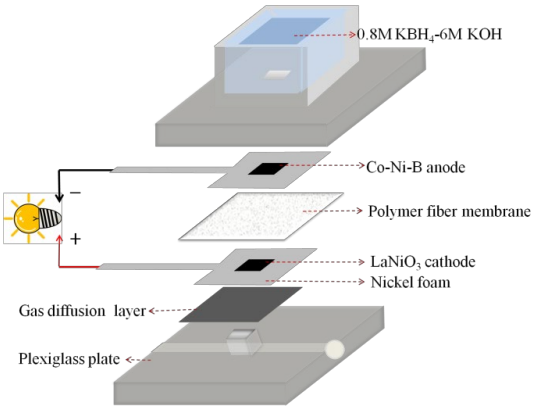

199

200 **Fig. 1-** The structure of DBFC.

201 The cathode is composed of a gas diffusion layer, an active layer, and a current
202 collector layer (nickel foam). The ink of the active layer was prepared by mixing 28
203 wt% of $LaNiO_3$ catalyst, 36 wt% of multi-walled carbon nanotubes (MWCNT), 36 wt%
204 of PTFE solution in ethanol under ultrasonic sound bath for 1 h. The resulting slurry
205 was pasted on Ni foam employed as a current collector and dried in vacuum oven at
206 80 °C for 2 h. The cathode was finally obtained by pressing the Ni foam with the
207 active layer and gas diffusion layer together at a pressure of 3 MPa. The loading of the
208 cathode catalyst was 7.5 mg/cm^2.

209 The anode consisted of a current collector layer and an active layer. Briefly, 75
210 wt% catalyst (Co-Ni-B, Co-B, Ni-B or PtRu/C) and 25 wt% PTFE solution in ethanol
211 solution were mixed to form a slurry by ultrasonic dispersion for 1 h. Then the slurry
212 was pasted on a Ni foam (the same to the cathode) and dried at 80 °C for 2 h. Finally,
213 the anode was pressed under a pressure of 2 MPa. The loading of the anode catalyst
214 was 30 mg/cm^2.

215 The performance of the DBFC was measured by discharging tests at room
216 temperature (~25 °C) using a battery testing system. The oxygen flow rate at the

cathode was 20 standard cm^3/s, and 0.8 M KBH_4-6 M KOH aqueous solution was supplied to the anode. The stability test of the battery is conducted as discharging with 80 mA/cm^2 current density. During this period, with the consumption of electrolyte, new electrolyte needs to be added.

3. Results and discussion

XRD pattern of Co-Ni-B, Ni-B and Co-B in Fig. 2a, displays a wide diffraction peak around $2\theta = 45°$, which indicates an amorphous structure for the catalysts. The morphology of the as-prepared Co-B and Ni-B were characterized using SEM, TEM and HRTEM. Fig. 2b is the TEM of Co-B, Fig. S3 and Fig. S4 show the SEM images and the average diameter of Co-B (23.3 nm). From the HRTEM image of Co-B in Fig. 2c, it's noted that the Co-B has short-range order and long-range disorder, which is a common characteristic of amorphous alloys, and the plane distance of 0.205 nm which can be assigned to the (211) plane of Co_xB. As shown in TEM (Fig. 2d) and SEM (Fig. S5) of the Ni-B, the average particle size of Ni-B is smaller than Co-B, with a diameter of 19.1 nm (Fig. S6). The corresponding HRTEM image in Fig. 2e shows that the characteristic of amorphous alloys and the plane distance of Ni-B is 0.194 nm can be assigned to the (211) plane of Ni_xB. Fig. 2f gives the SEM of Co-Ni-B catalyst display bundle of spherical nanocomposite composed with 2D ultrathin nano-sheets cluster on the surface with an average size of 344.1 nm (Fig. S7). In addition, it can clearly found that due to the fixed support of the central spheres, the nanosheets on its surface with a thickness of ~30 nm are not stacked together, and the catalytic materials inside are also well exposed (Fig. 2g). HRTEM image of Co-Ni-B

is shown in Fig. 2h, it further confirmed that the Co-Ni-B catalyst also has the characteristic of amorphous alloys, and this is consistent with the XRD results. The plane distance of 0.197 nm in Co-Ni-B is in agreement with the calculated value of approximately 0.2 nm, which is almost the same to the value calculated from the XRD pattern ($2\theta = 45°$), and can be assigned to the (211) plane of Co_xB or Ni_xB. Fig. 2i gives the HAADF-STEM image of Co-Ni-B catalyst. The elemental mapping of Co-Ni-B in Fig. 2j to 2n show an even distribution of Co, Ni, O and B. The signal intensity of O is weaker in the center than Co and Ni element, suggesting it is mainly distributed on the outer layer. The B is uniformly dispersed on the whole composite. According to the above results, it is confirmed that the center is mainly composed of Co and B elements, and the outer layer is mainly composed of Ni, O, B, and tiny Co elements.

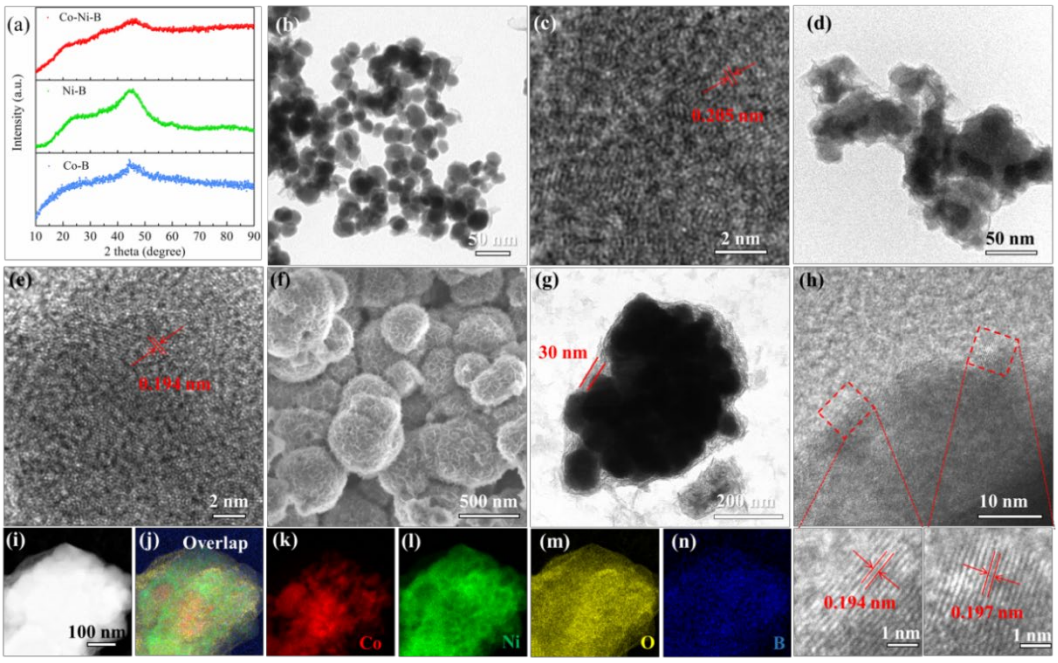

Fig. 2- (a) XRD pattern of Co-Ni-B, Ni-B and Co-B. (b) TEM and (c) HRTEM of Co-B. (d) TEM and (e) HRTEM of Ni-B. (f) SEM, (g) TEM, (h) HRTEM and the local enlarged images of Co-Ni-B. (i) HAADF-STEM and (j) overlap mapping image of Co-Ni-B, and elemental mapping of (k) Co, (l) Ni, (m) O, (n) B.

X-ray photoelectron spectroscopy (XPS) analysis of Co-Ni-B were carried out to investigate the elemental composition and chemical state of the surface. Fig. 3a reveals B 1s spectra with two peaks at 187.9 eV and 192.0 eV [39], corresponding to elemental B (zero oxidation state) and oxidized B (BO_2^-). BO_2^- is a byproduct of BH_4^- partial hydrolysis (as shown in Eq (2)), and has an adhesive effect [40]. In addition, the peak of O 1s at 531.3 eV is partially assigned to OH^- groups (Fig. 3b), as it is proven by infrared spectroscopy (Fig. S8).

$$BH_4^- + 2H_2O = BO_2^- + 4H_2 \quad (2)$$

Co $2p_{3/2}$ region spectrum (Fig. 3c) can be deconvoluted to three major peaks at 778.0, 781.2, 782.8 eV, and one satellite peak at 786.1 eV. The peaks at 778.0 eV are assigned to Co_xB [41], and the ones at 781.2 eV and 782.8 eV are associated with Co^{2+} [42, 43], in $Co(OH)_2$ and $Co(BO_2)_2$ respectively. The spectrum of Ni $2p_{3/2}$ (Fig. 3d) displays two major peaks at 852.9 eV and 856.1 eV, and one satellite at 861.7 eV [44], the binding energy of 852.9 eV corresponds to the energy level of Ni_xB, 856.1 eV is assigned to the Ni^{2+} [45], which corresponds to $Ni(OH)_2$ and $Ni(BO_2)_2$. According to the above results, the center composed of Co_xB and Ni_xB, the 2D nanosheets of $Ni(OH)_2$ and tiny amounts of $Co(OH)_2$ are planting on the surface of Co_xB and Ni_xB, which consistent with the result of the elemental mapping. $Ni(BO_2)_2$ and $Co(BO_2)_2$ make strong adhesion between Ni_xB (or Co_xB) and $Ni(OH)_2$ (or $Co(OH)_2$) and play a role of immobilizing 2D sheets. The results of XPS also suggest the electronic structure of the Co-Ni-B catalyst, comparison with that of Co-B and Ni-B, a significant positive shift of Co $2p_{3/2}$ and Ni$2p_{3/2}$ XPS signal (Fig. S9a, b and

Table S1, S2), due to the electron transfer from the neighboring Co and Ni atoms to B atoms. In parallel, the peaks of B1s of the Co-Ni-B negatively shifted comparing to that of the Co-B and Ni-B (Fig. S9c, Table S3), it also indicates that there are electrons transferred to B, which confirmed the downshift of the d-band center of Co, Ni in Co-Ni-B catalyst. Such downshift of the d-band center and by electron transfer through doping is more conducive to the improvement of the intrinsic activity of the catalyst materials, which could greatly accelerate the charge transfer process between OH^- and Co-Ni-B and significantly improve the activity for BOR [46-48]. In addition, the content of each element analyzed by ICP-MS can be found in Table S4.

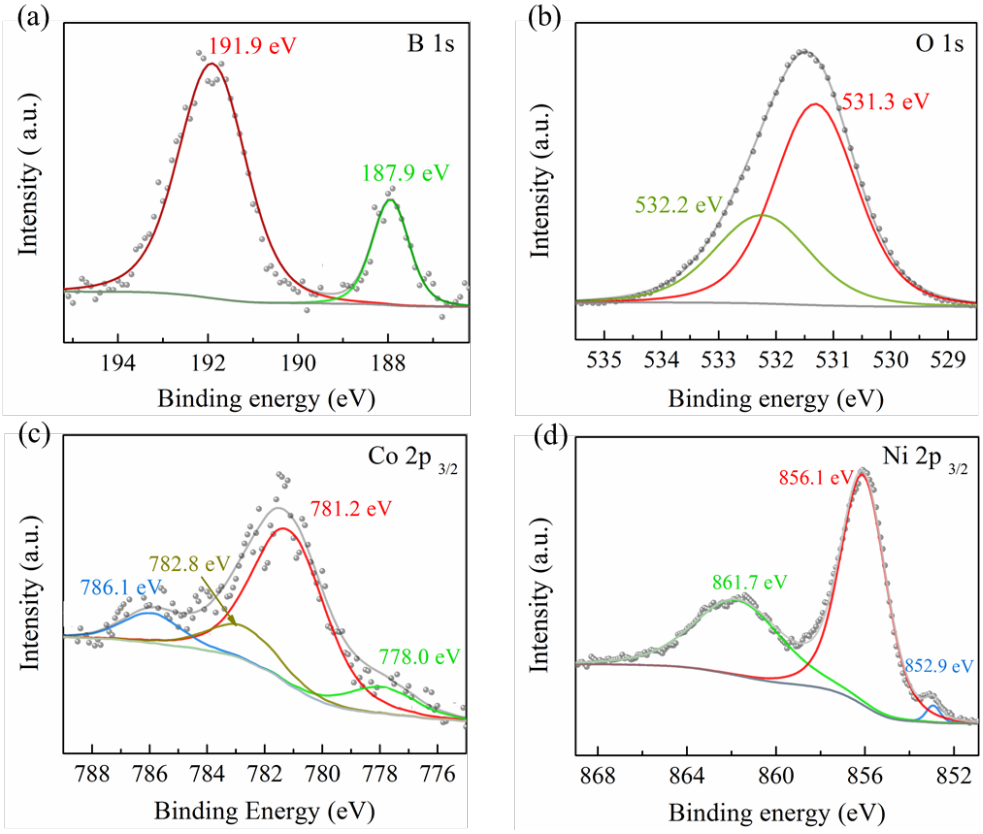

Fig. 3- High-resolution XPS of the Co-Ni-B on (a) B, (b) O, (c) Co, (d) Ni regions with the deconvoluted compounds. Dots indicates the experimental data.

The electrochemical behavior of Co-Ni-B electrode for KBH_4 electrooxidation was researched in a typical three-electrode system at room temperature ~25 °C. Fig.

4a shows the CVs of Co-Ni-B in absence and presence of KBH_4. Without KBH_4, the CV curve does not show apparent current density peaks, and the current density of Co-Ni-B is 1.4 mA/cm^2. In the presence of KBH_4, the CV curve exhibited higher current density (6.6 mA/cm^2 at 0.7 V *vs* Hg/HgO) on the Co-Ni-B electrode, which is caused by the electrooxidation of KBH_4 on the electrode. Co-Ni-B catalysts with different mole ratio of Co to Ni were prepared to select the best catalyst. Fig. 4b shows that the highest current density of Co-Ni-B, 6.6 mA/cm^2 can be achieved in Co-Ni-B=1:2:1 and this is the catalyst used thoroughly in this work. Fig. 4c presents the CV curves of Co-B, Ni-B, Co-Ni-B, PtRu/C and Pt/C in 0.1 M KBH_4-1M KOH. It can be seen that PtRu/C and Pt/C exhibit inferior catalytic activity for KBH_4 electrooxidation, whereas Co-B, Ni-B, and Co-Ni-B electrodes exhibit the highest current density of 6.6 mA/cm^2. According to reported literature, the initial oxidation potential of KBH_4 is around 0.45 V *vs* Hg/HgO [49]. Thus, the primary reaction, at the potential negative than 0.45 V, is the oxidation of BH_4^- hydrolyzed hydrogen. When the potential is positive than 0.45 V, the rapidly increased current density is related to the direct electrooxidation of BH_4^- which is caused by the electrooxidation of KBH_4 on the electrode. This phenomenon suggests that Co-Ni-B electrode possesses specific catalytic performance toward KBH_4 oxidation [50]. In Fig. 4d, the CA curves test in 0.1 M KBH_4-1 M KOH solution is used to evaluate further the electrocatalytic activity and operating stability of Co-B, Ni-B, Co-Ni-B and PtRu/C, and the current density of each catalyst is recorded at 0.6 V for 6000 s. In the initial stage the current density decays rapidly, which is attributed to the hydrolysis of BH_4^-

on the surface of the catalysts to form a limiting layer that gradually occupy the active sites. After 6000 s CA test, the current density of Co-Ni-B electrode was maintained at 40.48 mA/cm^2, which is the highest compared to the Co-B, Ni-B and PtRu/C catalysts, indicating that the Co-Ni-B catalyst shows excellent operating stability than other three catalysts [21], the details of processing are summarized in Table 1. The electrochemical active surface area (EASA) of the catalysts is educed from the double layer capacitance (C_d). CV curves, which recorded in 1 M KOH at non-Faraday potential windows of 0.5 to 0.6 V, are used to evaluate the EASA of prepared catalysts Co-B, Ni-B (Fig. S10) and Co-Ni-B (Fig. 4e). The corresponding relationship between V *vs*. *j* at 0.55 V was exhibited in Fig. 4f. Double-layer capacitance (C_d) of the catalyst could be estimated by Eq (3) and Eq (4) [51].

$$d_j = C_d . d_v \tag{3}$$

$$EASA = C_d / C^* \tag{4}$$

where C^* is the specific theoretical double layer capacitance, the C^* of Co and Ni in alkaline electrolyte is thought to be 60 μF/cm^2 [52]. The C_d on Co-B, Ni-B and Co-Ni-B catalysts were evaluated as 1.07 $\times 10^{-3}$ F/cm^2, 2.31$\times$ 10^{-4} F/cm^2 and 4.37$\times 10^{-3}$ F/cm^2. Based on Eq (4), the EASA value of the Co-B, Ni-B and Co-Ni-B catalysts are 17.8 cm^2, 3.85 cm^2 and 72.8 cm^2. The EASA of Co-Ni-B is 19 times larger than Ni-B catalyst, and 4 times larger than Co-B. The larger EASA achieved on Co-Ni-B catalyst may be caused by the nano-sheets structure of $Ni(OH)_2$ and $Co(OH)_2$.

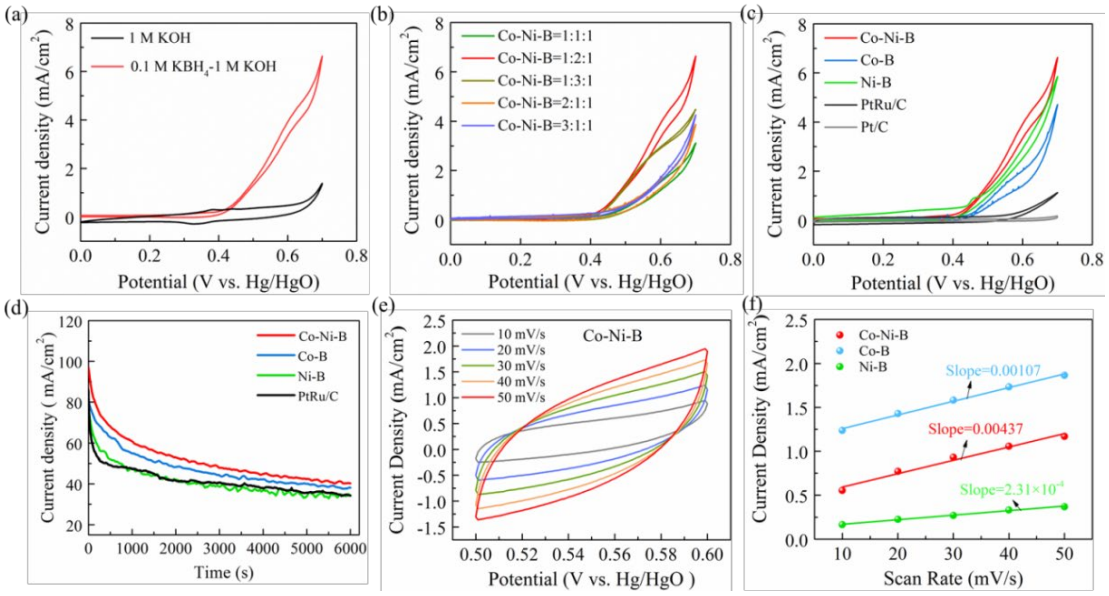

Fig. 4- (a) CVs of Co-Ni-B electrode in the situations of absence and presence of KBH_4, (b) CVs of Co-Ni-B in 0.1 M KBH_4-1 M KOH, (c) CVs of Co-B, Ni-B, Co-Ni-B, PtRu/C and Pt/C in 0.1 M KBH_4-1 M KOH. (d) Chronoamperogram of Co-B, Ni-B, Co-Ni-B and PtRu/C in 0.1 M KBH_4-1 M KOH solutions at a potential step of 0.6 V for 6000 s. (e) CV curves of Co-Ni-B catalyst under different scan rate. (f) Arrhenius plots of Co-B, Ni-B, Co-Ni-B catalysts.

Table 1-Summary of the current density for chronoamperogram.

Catalysts	Current density (mA/cm^2)
Co-B	37.98
Ni-B	34.09
PtRu/C	34.32
Co-Ni-B	40.48

To further investigate the electronic structure of the Co-Ni-B catalyst, investigated by UV-vis diffuse reflectance spectra (DRS) spectroscopic studies and the spectra are shown in Fig. 5a. The Tauc plot of transformed Kubelka-Munk function: $[F(R)hv]^{1/2}$ plotted against the energy of light hv is shown in Fig. 5b, the band gaps of the catalysts were determined from the reflectance spectra according to Eq (5) [53, 54].

$$F(R)hv = A(hv - E_g)^n \qquad (n = 1,2) \tag{5}$$

Where $F(R)$ is the diffuse reflectance absorption coefficient which can be calculated on the basis of the Kubella-Munk function [55]. The $h\nu$ is the photon energy, A is the proportional constant, and E_g is the band gap energy. The values of n represent the type of transition when n taken as 2 is the direct transition, taken 1/2 is the indirect transition. By the plot of $(F(R)h\nu)^{1/n}$ *vs.* hν, the intercept of $(F(R)h\nu)^{1/n}$ on the hν axis is the E_g value [56]. The value of Co-Ni-B, Co-B and Ni-B are given in Table S5, the band gap energy of Co-Ni-B is calculated to be 2.61 eV smaller than Co-B (3.30 eV) and Ni-B (3.17 eV). The narrower band gap of Co-Ni-B is attributed to the interaction of the components of $Co(OH)_2$, $Ni(OH)_2$, Ni_xB and Co_xB. The little band gap energy is more easily for electrons jump from the valence band to the conduction band and become free electrons [57], which can urge the charge transfer kinetic be greatly accelerated and obtain good BOR activities.

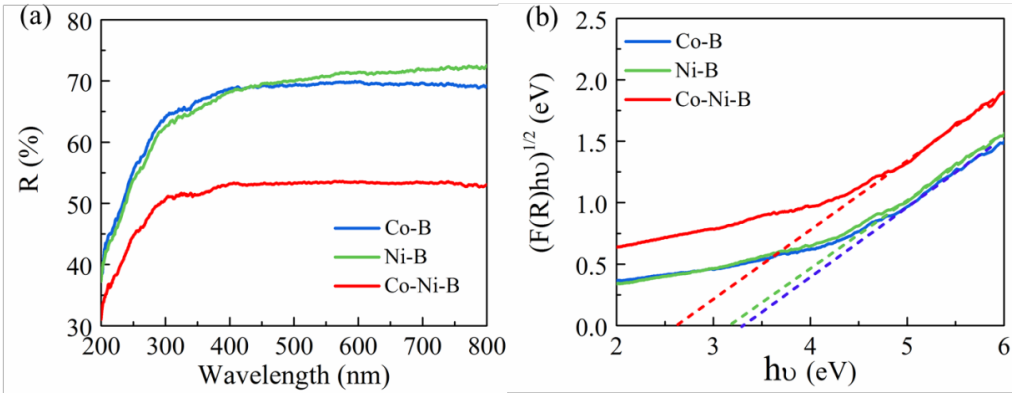

Fig. 5- (a) UV-vis diffuse reflectance spectra of Co-Ni-B, Co-B and Ni-B. (b) Band-gap evaluation from the plot of $(F(R)hv)^{1/2}$ *vs* hv for Co-Ni-B, Co-B and Ni-B.

To evaluate the performance of the Co-Ni-B catalyst in a practical application, we assembled a DBFC. As prepared Co-Ni-B electrode was employed as the anode catalyst, $LaNiO_3$ as the cathode catalyst of DBFC. Discharge curves and power density curves of DBFC (under room temperature ~25 °C) were shown in Fig. 6a. It

368 can be clearly observed that the Co-Ni-B presents the highest peak power density 203
369 mW/cm^2, also obtained a high open circuit voltage (OCV) of 1.06 V. As exhibited in
370 Fig. 6b, Co-Ni-B also delivers the highest peak power density relative to those of the
371 Co-B (117 mW/cm^2), Ni-B (162 mW/cm^2), and the OCV and power density of
372 Co-Ni-B catalyst is even superior to state-of-the-art PtRu/C (0.96 V, 93 mW/cm^2) and
373 Pt/C (0.94 V, 47 mW/cm^2) catalysts. The electrochemical tests show that the
374 performance of DBFC is very sensitive to catalyst loading. Thus, the DBFC
375 performance under various catalysts loading was studied. Fig. 6c reveals the peak
376 power density was improved from 30 to 209 mW/cm^2 with increasing catalyst loading
377 from 10 to 50 mg/cm^2. With the increase of catalyst loading to 70 mg/cm^2, the power
378 density began to decrease. Because such a high loading and the increased thickness is
379 detrimental to the mass and electron transfer.

380 Operating stability of the fuel cell is also important for evaluating the
381 performance of DBFC in practical applications. Stability tests of the DBFC were
382 reflected in Fig. 6d. It indicates that assembled DBFC with Co-Ni-B catalyst works
383 very stable at 80 mA/cm^2 for 45 h, the output voltage can be retaining 93.2%. With a
384 higher output voltage (0.83 V) than those of DBFC assembled using Co-B, Ni-B and
385 PtRu/C (Fig. S11). Furthermore, excellent discharge performance is related to the
386 charge transfer and solution resistance. Therefore, the electrochemical impedance
387 spectroscopy (EIS) was recorded at the OCV of DBFC from 100 kHz to 0.01 Hz. In
388 general, the intersection point between the curve and the actual axis reflects the high
389 frequency equivalent series resistance (R_s), which originates from the resistance of the

electrolyte solution, including connections of interfaces and electrode clips, while the diameter of semicircles of Nyquist plots corresponding to the charge transfer resistance (R_{ct}) [58, 59]. The values of R_s and R_{ct} have great influence on the electrocatalytic kinetics, usually a smaller value of R_s indicates a good combination of catalyst and collector, and smaller R_{ct} value indicates an expeditious charge transfer. As shown in Fig. S12, the inset is a partial enlarged view, the R_s value of that Co-Ni-B is about 0.3 Ω, almost the same as those of the other three samples. Besides, the R_{ct} value of Co-Ni-B was estimated to be 4.7 Ω, which is lower than Co-B (6.9 Ω), Ni-B (20 Ω) and PtRu/C (4.9 Ω). These results certify the low internal resistance and fast oxygen electrochemical redox for the DBFC assembled using Co-Ni-B catalyst [46].

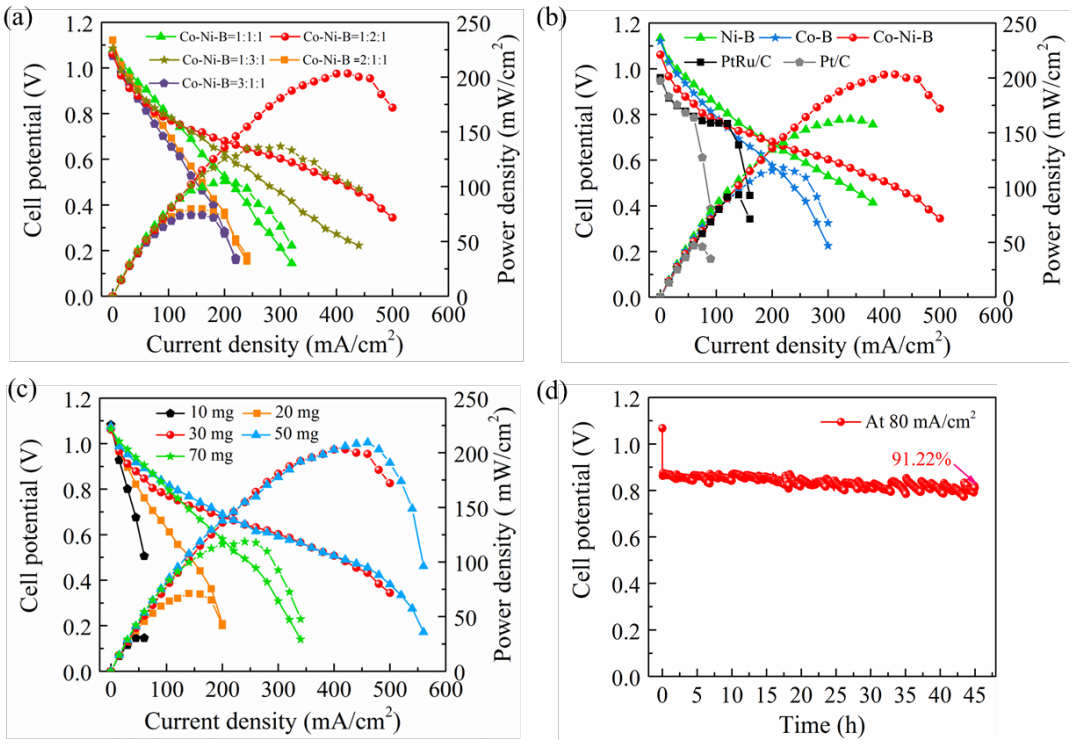

Fig. 6- The discharge polarization curves and power density curves of: (a) Co-Ni-B DBFCs, (b) DBFCs with catalysis of Co-B, Ni-B, Co-Ni-B, PtRu/C and Pt/C. (c) Co-Ni-B DBFC under different catalyst loading, (d) Stability test of DBFC at the 80 mA/cm^2 discharge current density.

4. Conclusion

An amorphous Co-Ni-B nanocomposite consists of nanoparticles and 2D structure has been successfully fabricated through a simple potassium borohydride reduction approach. It exhibits excellent BOR catalytic performance, high current density (6.6 mA/cm^2) during the reaction and good stability toward KBH_4 electrooxidation. While assembling in a DBFC, the OCV is as high as 1.06 V and peak power density is 209 mW/cm^2 achieved at room temperature. At the end of 45 h stability test, the fuel cell displays no obvious decay, which suggests that the assembled DBFC possesses excellent working stability. The special structure plays a key role in contributing to the catalytic performance, the enhanced synergetic effects could be ascribed to the narrow band gap accelerating the electrons jumping and therefore enhancing the speed of electron transfer.

Conflicts of interest

There are no conflicts to declare.

Acknowledgments

We gratefully acknowledge the financial support provided by the Natural Science Basic Research Program of Shaanxi (No.2018JQ2054) and the UK Engineering and Physical Sciences Research Council (EP/S032886/1).

References

[1] Qin HY, Lin LX, Chu W, Jiang W, He Y, Shi Q, et al. Introducing catalyst in alkaline membrane for improved performance direct borohydride fuel cells. J Power Sources 2018;374:113-120.

[2] Iqbal MZ, Rehman A-U, Siddique S. Prospects and challenges of graphene based fuel cells. J Energy Chem 2019;39:217-234.

[3] Braesch G, Bonnefont A, Martin V, Savinova ER, Chatenet M. Borohydride oxidation reaction mechanisms and poisoning effects on Au, Pt and Pd bulk electrodes: From model (low) to direct borohydride fuel cell operating (high) concentrations. Electrochim Acta 2018;273:483-494.

[4] Guo SQ, Sun J, Zhang ZY, Sheng AK, Gao M, Wang ZB, et al. Study of the electrooxidation of borohydride on a directly formed CoB/Ni-foam electrode and its application in membraneless direct borohydride fuel cells. J Mater Chem A 2017;5:15879-15890.

[5] Huang CC, Liu YL, Pan WH, Chang CM, Shih CM, Chu HY, et al. Direct borohydride fuel cell performance using hydroxide-conducting polymeric nanocomposite electrolytes. J Polym Sci Part B: Polym. Phys 2013;51:1779-1789.
[6] Sljukic B, Milikic J, Santos DMF, Sequeira CAC, Maccio D, Saccone A. Electrocatalytic performance of Pt-Dy alloys for direct borohydride fuel cells. J Power Sources 2014;272:335-343.
[7] Wang B, Wang GL, Cao DX, Ke Y, Cheng K, Zhu K, et al. A flexible and highly effective paper based gold electrode for sodium borohydride electrocatalysis. Int J Hydrogen Energy 2017;42:22814-22820.
[8] Atwan MH, Northwood DO, Gyenge EL. Evaluation of colloidal Ag and Ag-alloys as anode electrocatalysts for direct borohydride fuel cells. Int J Hydrogen Energy 2007;32:3116-3125.
[9] Hjelm RME, Garsany Y, Atkinson RW, Stroman RO, Swider-Lyons K, Lafforgue C, et al. Sodium borohydride oxidation on Pt and/or Pd-Based electrodes in hydrogen peroxide direct borohydride fuel cells (H_2O_2-DBFCs). ECS Transactions 2017;80:1033-1042.
[10] Cheng K, Jiang JT, Kong SY, Gao YY, Ye K, Wang GL, et al. Pd nanoparticles support on rGO-C@TiC coaxial nanowires as a novel 3D electrode for $NaBH_4$ electrooxidation. Int J Hydrogen Energy 2017;42:2943-2951.
[11] Milikic J, Ciric-Marjanovic G, Mentus S, Santos DMF, Sequeira CAC, Sljukic B. Pd/c-PANI electrocatalysts for direct borohydride fuel cells. Electrochim Acta 2016;213:298-305.
[12] Martins M, Sljukic B, Metin O, Sevim M, Sequeira CAC, Sener T, et al. Bimetallic PdM (M = Fe, Ag, Au) alloy nanoparticles assembled on reduced graphene oxide as catalysts for direct borohydride fuel cells. J Alloys Compd 2017;718:204-214.
[13] Ma J, Sahai Y, Buchheit RG. Direct borohydride fuel cell using Ni-based composite anodes. J Power Sources 2010;195:4709-4713.
[14] Hosseini MG, Mahmoodi R. Preparation method of Ni@Pt/C nanocatalyst affects the performance of direct borohydride-hydrogen peroxide fuel cell: Improved power density and increased catalytic oxidation of borohydride. J Colloid Interface Sci 2017;500:264-275.
[15] Wang J, Lin LX, He Y, Qin HY, Yan S, Yang K, et al. Vacancy-assisted oxygen reduction reaction on cobalt-based catalysts in direct borohydride fuel cell revealed by in-situ XAFS and XRD. Electrochim Acta 2017;254:72-78.
[16] Li S, Yang XD, Zhu HY, Liu Y, Liu YN. Hydrogen storage alloy and carbon nanotubes mixed catalyst in a direct borohydride fuel cell. J Mater Sci Technol 2011;27:1089-1093.
[17] Chen YZ, Zhou TF, Li L, Pang WK, He XM, Liu YN, et al. Interfacial engineering of nickel boride/metaborate and its effect on high energy density asymmetric supercapacitors. ACS Nano 2019;13:9376-9385.
[18] Yi LY, Liu L, Liu X, Wang XY, Yi W, He PY, et al. Carbon-supported Pt-Co nanoparticles as anode catalyst for direct borohydride-hydrogen peroxide fuel cell: Electrocatalysis and fuel cell performance. Int J Hydrogen Energy 2012;37:12650-12658.
[19] Li S, Yang XD, Zhu HY, Wei XZ, Liu YN. Ultrafine amorphous Co-W-B alloy as the anode catalyst for a direct borohydride fuel cell. Int J Hydrogen Energy 2013;38:2884-2888.
[20] Zhiani M, Mohammadi I. Performance study of passive and active direct borohydride fuel cell employing a commercial Pd decorated Ni-Co/C anode catalyst. Fuel 2016;166:517-525.
[21] Zhang DM, Wang GL, Yuan Y, Li YG, Jiang SP, Wang YK, et al. Three-dimensional functionalized graphene networks modified Ni foam based gold electrode for sodium borohydride electrooxidation. Int J Hydrogen Energy 2016;41:11593-11598.

[22] Merino-Jimenez I, de Leon CP, Shah AA, Walsh FC. Developments in direct borohydride fuel cells and remaining challenges. J Power Sources 2012;219:339-357.
[23] Finkelstein DA, Letcher CD, Jones DJ, Sandberg LM, Watts DJ, Abruna HD. Self-Poisoning during BH_4^- oxidation at Pt and Au, and in situ poison removal procedures for BH_4^- fuel cells, J Phys Chem C 2013;117:1571-1581.
[24] Lota G, Sierczynska A, Acznik I, Lota K. AB(5)-type hydrogen storage alloy modified with carbon used as anodic materials in borohydride fuel cells. Int J Electrochem Sci 2014;9:659-669.
[25] Atwan MH, Northwood DO, Gyenge EL. Evaluation of colloidal Ag and Ag-alloys as anode electrocatalysts for direct borohydride fuel cells. Int J Hydrogen Energy 2007;32:3116-3125.
[26] Wang QY, Luo YM, Hou RZ, Zaman S, Qi K, Liu HF, et al. Redox tuning in crystalline and electronic structure of bimetal-organic frameworks derived cobalt/nickel boride/sulfide for boosted faradaic capacitance. Adv Mater 2019;31:201905744.
[27] Masa J, Weide P, Peeters D, Sinev I, Xia W, Sun ZY, et al. Amorphous cobalt boride (Co_2B) as a highly efficient nonprecious catalyst for electrochemical water splitting:oxygen and hydrogen evolution. Adv Energy Mater 2016;6:1502313.
[28] Tan T, Han PY, Cong HJ, Cheng GZ, Luo W. An Amorphous cobalt borate nanosheet-coated cobalt boride hybrid for highly efficient alkaline water oxidation reaction. ACS Sustain Chem Eng 2019;7:5620-5625.
[29] Li S, Shu CY, Chen YZ, Wang LN. A new application of nickel-boron amorphous alloy nanoparticles: anode-catalyzed direct borohydride fuel cell. Ionics 2017;24:201-209.
[30] Sun JC, Feng S, Wang XJ, Zhang GZ, Luo Y, Jiang J. Regulation of electronic structure of graphene nanoribbon by tuning long-range dopant-dopant coupling at distance of tens of nanometers. J Phys Chem Lett 2020;11:6907-6913.
[31] Suter JL, Sinclair RC, Coveney PV. Principles governing control of aggregation and dispersion of graphene and graphene oxide in polymer melts. Adv Mater 2020;32:2003213.
[32] Mannix AJ, Zhang ZH, Guisinger NP, Yakobson BI, Hersam MC. Borophene as a prototype for synthetic 2D materials development. Nat Nanotechnol 2018;13:444-450.
[33] Kiraly B, Liu XL, Wang LQ, Zhang ZH, Mannix AJ, Andrew J, et al. Borophene synthesis on Au(111). ACS Nano 2019;13:3816-3822.
[34] Tang X, Guo X, Wu WJ, Wang GX. 2D Metal carbides and nitrides (MXenes) as high-performance electrode materials for lithium-based batteries. Adv Energy Mater 2018;8:1801897.
[35] Xu CX, Fan CC, Zhang XL, Chen HT, Liu XT, Fu ZM. et al. MXene (Ti_3C_2Tx) and carbon nanotube hybrid-supported platinum catalysts for the high-performance oxygen reduction reaction in PEMFC. ACS Appl Mater Interfaces 2020;12:19539-19546.
[36] Wang JJ, Ye TN, Gong YT, Wu JZ, Miao NX, Tada T, et al. Discovery of hexagonal ternary phase Ti_2InB_2 and its evolution to layered boride TiB. Nat Commun 2019;10:2284.
[37] Rosli NF, Nasir MZM, Antonatos N, Sofer Z, Dash A, Gonzalez-Julian J, et al. MAX and MAB Phases: Two-dimensional layered carbide and boride nanomaterials for electrochemical applications. ACS Appl Nano Mater 2019;2:6010-6021.
[38] Forslund RP, Mefford JT, Hardin WG, Alexander CT, Johnston KP, Stevenson KJ. Nanostructured $LaNiO_3$ perovskite electrocatalyst for enhanced urea oxidation. ACS Catal 2016;6:5044-5051.
[39] Pan YX, Hu GH, Lu JT, Xiao L, Zhuang L. $Ni(OH)_2$-Ni/C for hydrogen oxidation reaction in alkaline media. J Energy Chem 2019;29:111-115.

[40] Chen YZ, Zhou TF, Li L, Pang WK, He XM, Liu YN, et al. Interfacial engineering of nickel boride/metaborate and its effect on high energy density asymmetric supercapacitors. ACS Nano 2019;13:9376-9385.
[41] Li D, Liu QY, Zhu CH, Wang HY, Cui CH, Wang CG, et al. Selective hydrogenolysis of 5-hydroxymethylfurfural to 2,5-dimethylfuran over Co_3O_4 catalyst by controlled reduction. J Energy Chem 2019;30:34-41.
[42] Ding DN, Shen K, Chen XD, Chen HR, Chen JY, Fan T, et al. Multi-level architecture optimization of MOF-templated Co-based nanoparticles embedded in hollow N-doped carbon polyhedra for efficient OER and ORR. ACS Catal 2018;8:7879-7888.
[43] Zhao YQ, Jin B, Zheng Y, Jin HY, Jiao Y, Qiao SZ. Charge state manipulation of cobalt selenide catalyst for overall seawater electrolysis. Adv Energy Mater 2018;8:1801926.
[44] Zhang X, Luo JS, Tang PY, Morante JR, Arbiol J, Xu CL, et al. Ultrasensitive binder-free glucose sensors based on the pyrolysis of in situ grown Cu MOF. Sens Actuators B 2018;254:272-281.
[45] Zhang GX, Jia Y, Zhang C, Xiong XY, Sun K, Chen RD, et al. A general route via formamide condensation to prepare atomically dispersed metal–nitrogen-carbon electrocatalysts for energy technologies. Energy Environ Sci 2019;12:1317-1325.
[46] Tian YM, Yu J, Zhang HS, Wang C, Zhang ML, Lin ZW, et al. 3D porous Ni-Co-P nanosheets on carbon fiber cloth for efficient hydrogen evolution reaction. Electrochim Acta 2019;300:217-224.
[47] Dubale AA, Zheng YY, Wang HL, Hubner R, Li Y, Yang J, et al. High-performance bismuth-doped nickel aerogel electrocatalyst for methanol oxidation reaction. Angew Chem Int Ed 2020;59:13891-13899.
[48] Liu XT, Yu EH, Scott K. Preparation and evaluation of a highly stable palladium yttrium platinum core-shell-shell structure catalyst for oxygen reduction reactions. Appl Catal B Environ 2015;162:593-601.
[49] Wang J, Liu W, Luo G, Li ZJ, Zhao C, Zhang HR, et al. Synergistic effect of well-defined dual sites boosting the oxygen reduction reaction. Energy Environ Sci 2018;11:3375-3379.
[50] Li BP, Song CY, Huang XM, Ye K, Cheng K, Zhu K, et al. A novel anode for direct borohydride-hydrogen peroxide fuel cell: Au nanoparticles decorated 3D self-supported reduced graphene oxide foam. ACS Sustain Chem Eng 2019;7:11129-11137.
[51] Trasatti S, Petrii OA. Real surface area measurements in electrochemistry. J Electroanal Chem 1992;327:353-376.
[52] Guo F, Cao DX, Du MM, Ye K, Wang GL, Zhang WP, et al. Enhancement of direct urea-hydrogen peroxide fuel cell performance by three-dimensional porous nickel-cobalt anode. J Power Sources 2016;307:697-704.
[53] Yang CM, Gao GM, Guo ZF, Song LT, Chi JZ, Gan SC. Two-step hydrothermal synthesis of novel hierarchical $Co_3O_4/Bi_2O_2CO_3$ p-n heterojunction composite photocatalyst with enhanced visible light photocatalytic activity. Appl Surf Sci 2017;400:365-374.
[54] Zhu YP, Zhu RL, Zhu GQ, Wang MM, Chen YN, Zhu JX, et al. Plasmonic Ag coated Zn/Ti-LDH with excellent photocatalytic activity. Appl Surf Sci 2018;433:458-467.
[55] Orel ZC, Gunde MK, Orel B. Application of the kubelka-munk theory for the determination of the optical properties of solar absorbing paints. Prog Org Coat 1997;30:59-66.
[56] D'Amato CA, Giovannetti R, Zannotti M, Rommozzi E, Ferraro S, Seghetti CM. et al. Enhancement of visible-light photoactivity by polypropylene coated plasmonic Au/TiO_2 for dye degradation in water solution. Appl Surf Sci 2018;441:575-587.

[57] Liu Y, Chen YZ, Li S, Shu CY, Fang Y, Song B. Improved charge transfer in a Mn_2O_3@$Co_{1.2}Ni_{1.8}O_4$ hybrid for highly stable alkaline direct methanol fuel cells with good methanol tolerance. ACS Appl Mater Interfaces 2018;10:9485-9494.

[58] Chen YZ, Pang WK, Bai HH, Zhou TF, Liu YN, Li S, et al. Enhanced structural stability of nickel-cobalt hydroxide via intrinsic pillar effect of metaborate for high-power and long-life supercapacitor electrodes. Nano Lett 2017;17:429-436.

[59] Zou KY, Li N, Dai X, Jing WT, Shi M, Lu CJ, et al. Lightweight freestanding CeF_3 nanorod/carbon nanotube composite interlayer for lithium-sulfur batteries. ACS Appl Nano Mater 2020;3:5732-5742.